J Intel Connect Veh

Research Article

Control design for intelligent and connected vehicle swarm systems: A generalized Udwadia–Kalaba approach

Xiaomin Zhao[1], Bingwen Wang[1] , Xinhua Gao[1,2,✉], Weilong Hu[1,2], Ye-Hwa Chen[3]

Cite this article: https://doi.org/10.26599/JICV.2026.9210096

ABSTRACT: This paper investigates safe formation control of intelligent and connected vehicle swarm (ICVS) systems in obstacle-rich environments with nonlinear dynamics, bounded safety constraints, and model uncertainties. First, a constraint-oriented modeling framework is developed for ICVS systems, in which artificial potential field (APF) functions describe obstacle evasion and inter-agent collision avoidance, while formation deformation and recovery are integrated into a unified constrained-motion objective. Second, a generalized Udwadia–Kalaba (GUK) approach with diffeomorphism-based transformed constraints is applied to the constrained vehicle swarm system. The diffeomorphic transformation maps bounded inter-vehicle distance constraints into unconstrained variables, thereby supporting spacing regulation for both fixed and time-varying reference distances. Third, an adaptive robust controller is designed to achieve obstacle avoidance, collision avoidance, formation adjustment, and trajectory following in the presence of model uncertainties and external disturbances. The adaptive robust controller (ARC) is further compared with an LQR-based controller under the same constraint-following framework. Simulation results show that ARC produces smaller constraint errors and stronger disturbance attenuation while maintaining safe cooperative motion.

KEYWORDS: Intelligent and connected vehicles, Vehicle swarm systems, Generalized Udwadia-Kalaba approach, Constraint following, Adaptive robust control.

Nomenclature

$\boldsymbol{q}_i$	Generalized coordinate vector of the i-th ICV (m, m, rad)
$x_i \mid y_i$	Planar coordinates of the i-th ICV (m)
ψ_i	Heading angle of the i-th ICV (rad)
N_v	Number of intelligent and connected vehicles (–)
$\boldsymbol{p}_i$	Planar position vector of the i-th ICV (m)
$\boldsymbol{p}_a(t)$	Reference attraction point on the desired trajectory (m)
$\boldsymbol{p}_k^o$	Position vector of the k-th static obstacle (m)
N_o	Number of static obstacles (–)
d_{ij}	Distance between vehicles i and j (m)
d_{ik}^o	Distance between vehicle i and obstacle k (m)
$\underline{d} \mid \overline{d}$	Lower and upper bounds of the inter-vehicle distance (m)
$\underline{d}_o \mid \overline{d}_o$	Minimum obstacle safety distance and obstacle-repulsion activation radius (m)
$\boldsymbol{f}_i$	Artificial-potential-field guidance vector of vehicle i (m·s⁻¹)
$\boldsymbol{f}_i^a$	Attraction-guidance component (m·s⁻¹)

$\boldsymbol{f}_i^v$	Inter-vehicle avoidance and cohesion guidance component (m·s⁻¹)
$\boldsymbol{f}_i^o$	Obstacle-repulsion guidance component (m·s⁻¹)
$f_i^x \mid f_i^y$	x- and y-components of the guidance vector (m·s⁻¹)
k^a	Attraction gain (s⁻¹)
$\underline{k}^v \mid \overline{k}^v$	Lower-bound collision-avoidance and upper-bound cohesion gains (model-dependent)
k^o	Obstacle-repulsion gain (model-dependent)
ψ_i^a	APF-induced desired heading angle (rad)
λ_a	Heading-convergence gain (s⁻¹)
$\boldsymbol{A}$	Constraint coefficient matrix (–)
$\boldsymbol{b}_i$	Velocity-level heading-constraint term (rad·s⁻¹)
$\boldsymbol{d}^v$	Adjacent-vehicle distance vector (m)
$\boldsymbol{d}_f$	Reference inter-vehicle distance vector (m)
$\boldsymbol{e}_v$	Inter-vehicle distance-error vector (m)
$\underline{\boldsymbol{e}}_v \mid \overline{\boldsymbol{e}}_v$	Lower and upper bounds of the distance-error vector (m)
$\boldsymbol{\eta}$	Normalized distance-error vector (–)
$\boldsymbol{\xi}$	Diffeomorphically transformed error vector (–)
$\boldsymbol{K}_p$	Proportional gain matrix of the transformed-error dynamics (s⁻²)

[1] School of Automotive and Transportation Engineering, Hefei University of Technology, Hefei 230009, China. [2] Chery Automobile Co., Ltd., Wuhu 241000, China. [3] George W. Woodruff School of Mechanical Engineering, Georgia Institute of Technology, Atlanta GA 30332, USA.

✉ Corresponding author. E-mail: gaoxinhua@hfut.edu.cn

Received: July 20, 2026; Revised: August 9, 2026; Accepted: August 19, 2026

$\boldsymbol{K}_d$	Derivative gain matrix of the transformed-error dynamics (s^{-1})
$\boldsymbol{\tau}$	Total generalized control input (N, N, N·m)
$\boldsymbol{\tau}_g$	Nominal generalized Udwadia–Kalaba control term (N, N, N·m)
$\boldsymbol{\tau}_s$	Constraint-error stabilizing control term (N, N, N·m)
$\boldsymbol{\tau}_r$	Adaptive robust compensation term (N, N, N·m)
$\boldsymbol{M}$	Inertia matrix of the ICV system (mixed SI)
$\boldsymbol{C}$	Coriolis–centrifugal matrix (mixed SI)
$\boldsymbol{b}_a$	Acceleration-level constraint term (rad·s^{-2})
$\boldsymbol{\Gamma}$	Nominal constraint-following acceleration vector (m·s^{-2}, rad·s^{-2})
$\boldsymbol{\chi}$	Null-space projection matrix (–)
$\boldsymbol{\mu}$	Auxiliary acceleration input (m·s^{-2}, rad·s^{-2})
$\boldsymbol{h}_1$	Drift term of the transformed constraint dynamics (s^{-2})
$\boldsymbol{h}_2$	Input mapping of the transformed constraint dynamics (model-dependent)
H_1	Range space of the transformed-constraint input mapping (–)
H_2	Null space of the transformed-constraint input mapping (–)
$\boldsymbol{\nu}$	Null-space secondary input (m·s^{-2}, rad·s^{-2})
$\boldsymbol{\tau}_{g_1}$	Nominal constraint-following control component (N, N, N·m)
$\boldsymbol{\tau}_{g_2}$	Auxiliary transformed-constraint control component (N, N, N·m)
$\boldsymbol{\beta}$	Velocity-level constraint-error vector (rad·s^{-1})
k_β	Constraint-error feedback gain (s^{-1})
$\boldsymbol{P}$	Positive-definite weighting matrix (–)
$\overline{\boldsymbol{M}} \mid \overline{\boldsymbol{C}}$	Nominal inertia and Coriolis–centrifugal matrices (mixed SI)
$\Delta\boldsymbol{M} \mid \Delta C$	Uncertain parts of the dynamic matrices (mixed SI)
$\boldsymbol{\sigma}$	Uncertain parameter vector (–)
$\boldsymbol{\Sigma}$	Unknown compact set of uncertain parameters (–)
$\boldsymbol{D}$	Nominal inverse-inertia matrix (mixed SI)
$\Delta\boldsymbol{D}$	Inverse-inertia mismatch matrix (mixed SI)
$\boldsymbol{E}$	Dimensionless inverse-inertia error matrix (–)
$\boldsymbol{\Xi}$	Auxiliary robustness matrix (–)
λ_E	Lower bound associated with the symmetric part of the robustness matrix (–)
Π	Continuous uncertainty-bound function (model-dependent)
α	Unknown positive parameter vector of the uncertainty bound (–)
Π	Known basis-function vector for the uncertainty bound (–)
ω	Sinusoidal smoothing factor (–)
ε_ω	Smoothing threshold of the adjustment factor (–)
α	Adaptive estimate of the uncertainty-bound parameter vector (–)
k_1	Adaptive-law gain (model-dependent)
k_2	Leakage coefficient in the adaptive law (s^{-1})
$\boldsymbol{\zeta}$	Transformed constraint-state vector (–)
e_α	Uncertainty-bound parameter-estimation error (–)

$\boldsymbol{z}$	Augmented closed-loop error vector (–)
$\boldsymbol{A}_\xi$	State matrix of the transformed-error dynamics (s^{-1})
$\boldsymbol{R}_\xi$	Positive-definite Lyapunov matrix (–)
$\boldsymbol{Q}_\xi$	Positive-definite matrix in the Lyapunov equation (–)
$\boldsymbol{V}$	Lyapunov candidate function (–)
γ	Upper bound of the basis-function norm (–)
耨$_1$ | $_2$ | ?$_3$	Coefficients in the Lyapunov-derivative upper bound (model-dependent)
$\vartheta_1 \mid \vartheta_2$	Lower and upper Lyapunov comparison constants (–)
$r_0 \mid r_c \mid \underline{r} \mid \overline{r}$	Initial, critical, lower ultimate, and selected ultimate radii (–)
$\boldsymbol{L}(r_0)$	Uniform bound determined by the initial radius (–)
$T(\overline{r}, r_0)$	Finite convergence time to the ultimate bound (s)
$\boldsymbol{P}_0$	Initial-position matrix of the four ICVs (m)
$\boldsymbol{P}^{\mathrm{o}}$	Obstacle-position matrix used in simulation (m)
r_{o}	Radius of a circular obstacle (m)
$\boldsymbol{P}^{\mathrm{a}}$	Point matrix used to generate the attractive trajectory (m)
m_i	Mass of the i-th ICV (kg)
I_i	Yaw moment of inertia of the i-th ICV (kg·m²)
ℓ_i	Distance from the center of mass to the rear axle (m)
Y_i	Velocity-coupling scalar in the dynamic model (N)
$\boldsymbol{T}_i$	Wheel-torque-to-generalized-force mapping matrix (mixed SI)
$\boldsymbol{u}_i$	Left/right wheel-torque input vector (N·m)
r_i	Wheel radius (m)
ℓ_i^{w}	Lateral distance from each wheel to the vehicle centerline (m)
$u_i^L \mid u_i^R$	Left- and right-wheel torques (N·m)
$\overline{m}_i \mid \overline{\mathrm{I}}_i$	Nominal mass and nominal yaw moment of inertia (kg, kg·m²)
$\Omega_{xi} \mid \Omega_{yi}$	External disturbance forces in the x- and y-directions (N)
$\Omega_{\psi i}$	External disturbance moment in the heading direction (N·m)
d_{f_1}	Fixed reference inter-vehicle distance (m)
W_i^β	Accumulated sliding-variable error index (rad)
$\overline{W}_d$	Averaged formation-distance error index (m)
$d_{f_2}(t)$	Cosine-type time-varying desired distance (m)
$d_{f_3}(t)$	Exponential-type time-varying desired distance (m)

1. Introduction

Intelligent and connected vehicle swarm (ICVS) systems coordinate multiple connected and autonomous vehicles through information sharing and cooperative motion. Their autonomy, scalability, and collective capability make them promising for intelligent transportation and other tasks requiring coordinated mobility. Formation control is a fundamental problem in ICVS coordination because it enables multiple vehicles to maintain prescribed geometric relationships while moving as a group. Chen (2008) investigated the boundedness, convergence, and control of artificial swarm systems. Hwang and Abebe (2022) developed finite-time formation-tracking control for generalized heterogeneous multi-agent systems, whereas Chu et al. (2024) reviewed multi-vehicle consensus under uncertain communication networks. Cai et al. (2022) applied multi-vehicle formation control to flexible-lane unsignalized intersections, and Axelsson (2017) systematically reviewed safety issues in vehicle platooning. These studies provide effective coordination mechanisms when the prescribed formation remains feasible. In confined or obstacle-rich environments, however, a fixed formation may become temporarily infeasible. Vehicles must then avoid obstacles and inter-vehicle collisions, deform the formation when necessary, and recover the nominal formation after leaving the constrained region. These coupled requirements make safe formation control more difficult than conventional formation tracking or platoon stabilization. Therefore, deformation and recovery should also be considered in safe formation control. Fig. 1 shows the considered ICVS system.

Fig. 1. Schematic of the ICVS system.

Collision risks may arise from environmental obstacles, neighboring vehicles, and abrupt changes in the available workspace. Q. Dong et al. (2023) developed graph-based scenario-adaptive lane-changing trajectory planning for autonomous vehicles. Gao et al. (2025) introduced behavior-constrained multi-agent reinforcement learning for cooperative vehicle control at intersections. Q. Liu et al. (2025) investigated conflict-risk prediction in highway maintenance areas, whereas Y. Liu et al. (2025) developed proactive longitudinal control to assist lane changes in mixed traffic. Recent advances in interactive autonomous driving were reviewed by Y. Yang et al. (2025), and Zheng et al. (2025) proposed an emergency collision-avoidance method based on phase-plane regression regions. Although these studies improve safety in specific driving scenarios, obstacle avoidance, inter-vehicle collision avoidance, and formation adjustment are frequently treated as separate planning or control tasks. Artificial potential field (APF) methods are attractive because attractive and repulsive interactions can be represented in a compact form. Yamashita et al. (2003) applied motion planning to cooperative manipulation and transportation by multiple mobile robots, whereas Pizetta et al. (2019) used repulsive interactions to avoid obstacles during cooperative load transportation. Nevertheless, APF terms are commonly introduced as auxiliary guidance forces or local path corrections rather than being incorporated into a unified dynamics-based formulation. Consequently, obstacle avoidance, inter-vehicle collision avoidance, formation deformation, and formation recovery are often implemented through separate components without a common constraint representation.

The Udwadia–Kalaba (U–K) equation provides an explicit description of constrained mechanical motion and offers a direct basis for constraint-oriented control design. Udwadia et al. (1997) derived the equations of motion for constrained mechanical systems from the extended D'Alembert principle. Udwadia and Kalaba (2002a, 2002b) subsequently examined the foundations of analytical dynamics and the general explicit form of constrained equations of motion, whereas Udwadia (2023) presented the general Gauss principle of least constraint. Within this framework, desired system behaviors can be expressed as motion constraints, and the corresponding constraint force can be obtained explicitly. This property makes the U–K framework suitable for converting coordination and safety requirements into a dynamics-consistent control formulation. R. Zhao et al. (2020) developed U–K constraint-based tracking control for artificial swarm mechanical systems. C. Wang et al. (2021) applied the U–K approach to synchronization control of networked mobile robots. Zhu et al. (2023) extended the generalized U–K approach to robust constraint-following control of uncertain mechanical systems, whereas P. Liu et al. (2024) developed distributed formation-containment control for networked mobile robots. However, most conventional U–K formulations focus on equality constraints, prescribed trajectories, or fixed geometric relationships, whereas inter-vehicle safety requirements are naturally expressed as inequality constraints. Zhang et al. (2024) developed a generalized U–K control method for inequality-constrained systems, and Lu et al. (2024) used a diffeomorphism-based transformation to handle bounded saturation constraints. Such transformations map bounded physical variables into unconstrained coordinates so that regulation of the transformed variables maintains the original variables within their admissible ranges. Nevertheless, the combined use of diffeomorphic constraint transformation, APF-based safety guidance, and generalized U–K dynamics for ICVS systems with fixed or time-varying formation spacing remains insufficiently investigated.

Model uncertainties and external disturbances introduce an additional challenge. Vehicle motion may be affected by uncertain parameters, tire–ground interactions, tire slip, unmodeled nonlinearities, actuator imperfections, and environmental disturbances. Sun et al. (2023) developed adaptive robust formation control for connected and autonomous vehicle swarms, whereas S. Yang et al. (2025) investigated robust constraint-following control for uncertain networked multi-agent systems. P. Dong et al. (2025) developed continuous-integral-sliding-mode path-tracking control for intelligent vehicles equipped with wheel modules. Li et al. (2025) proposed an adaptive-neural-network-based hierarchical path-tracking method considering parametric uncertainties and tire slip, whereas Z. Yang et al. (2022) designed fuzzy robust path-tracking control for autonomous vehicles. Prescribed-performance, game-theoretic adaptive robust, and compensation-based methods provide additional tools for regulating transient behavior and suppressing uncertain dynamics. F. Wang et al. (2024) developed prescribed-performance adaptive robust control for robotic manipulators, Yin et al. (2025) investigated prescribed-performance trajectory tracking for uncertain nonholonomic mechanical systems, Zhao et al. (2026) developed a fuzzy-theoretic cooperative game framework for adaptive robust control of air–ground vehicle systems, and Z. L. Zhao et al. (2021) developed compensation-signal-driven control for uncertain nonlinear systems. Classical robust-control results established by Chen (1996), Chen and Zhang (2010), and Corless and Leitmann (1981) provide boundedness and performance guarantees for uncertain systems. For safe ICVS formation control, however, uncertainty compensation must be coordinated explicitly with obstacle-clearance regulation, inter-vehicle distance constraints, formation deformation, and formation recovery. These requirements are still frequently designed as separate components, which makes it difficult to provide a unified closed-loop interpretation of the complete maneuver.

To address these limitations, this paper develops a constraint-oriented adaptive robust control framework for uncertain ICVS systems operating in obstacle-rich environments. APF-based guidance, inter-vehicle safety requirements, and formation-adjustment objectives are formulated as coupled motion constraints. A diffeomorphic transformation converts bounded inter-vehicle distance constraints into unconstrained regulation variables, allowing the transformed constraints to be incorporated into a generalized U–K dynamics formulation. Based on this formulation, an adaptive robust controller is developed to achieve constraint following while compensating for uncertain dynamics. The main contributions of this paper are summarized as follows:

- **Constraint-oriented ICVS formation formulation:** The performance objectives of ICVS systems are transformed into motion constraint expressions that are isomorphic to physical constraints. Then, a unified constraint-oriented framework is constructed for ICVS systems, integrating inter-agent collision avoidance, obstacle evasion, formation deformation and recovery, and casting coupled coordination and safety requirements as motion constraints.
- **Generalized Udwadia–Kalaba modeling approach:** A generalized Udwadia–Kalaba dynamics formulation with a diffeomorphic constraint transformation is derived. The transformation maps bounded physical constraints to unconstrained variables while preserving the physical meaning of inter-agent distance constraints and supports both fixed and time-varying formation spacing within the constraint-following dynamics.
- **Adaptive robust constraint-following control:** Based on the derived dynamics model, an adaptive robust control scheme is developed for uncertain ICVS systems by combining constraint following, transformed-constraint regulation, and robust compensation to realize constrained motion and disturbance suppression, and the closed-loop properties are analyzed.

The remainder of this paper is organized as follows: Section 2 presents the ICV motion constraint formulation and APF-based guidance constraint. Section 3 introduces the generalized Udwadia–Kalaba approach. Section 4 derives the GUK-based adaptive robust controller and proves closed-loop stability. Section 5 presents the simulation design and results. Finally, Section 6 concludes the paper.

2. ICV motion constraint formulation

Consider a fleet of N_v intelligent and connected vehicles (ICVs) operating in a planar workspace. A centralized architecture with a connected V2V communication graph is adopted. Vehicle states are shared via V2V, the reference trajectory is provided via V2I, and static obstacle information is obtained via V2I or onboard sensing or prior maps. Ideal communication without delay or packet loss is assumed. The generalized coordinates of the i-th ICV are defined as

$$\boldsymbol{q}_i = \begin{bmatrix} x_i & y_i & \psi_i \end{bmatrix}^{\top} \in \mathbb{R}^3, \quad i = 1, 2, \ldots, N_v. \tag{1}$$

The ICVS system is required to satisfy the following motion requirements.

- **Collision avoidance:** Each ICV is required to maintain prescribed minimum safety distances from obstacles and neighboring vehicles.
- **Cooperative formation:** The ICVS is required to maintain or recover the desired relative configuration.

The above requirements are formulated as motion constraints for controller design. The APF provides avoidance-oriented guidance, whereas the diffeomorphic transformation enforces bounded adjacent-vehicle distance constraints. A schematic diagram of this constraint logic is presented in Fig. 2.

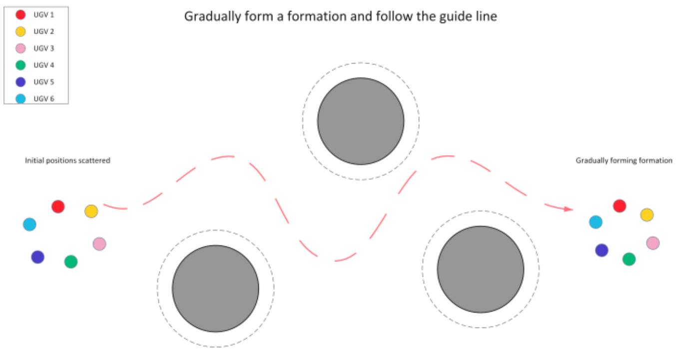

Fig. 2. Schematic diagram of cooperative formation tracking.

The planar position of the i-th ICV, the position of the k-th static obstacle, and the reference attraction point on the desired trajectory are defined as

$$\boldsymbol{p}_i = \begin{bmatrix} x_i & y_i \end{bmatrix}^{\text{晦}}, \quad \boldsymbol{p}_a(t) = \begin{bmatrix} x_a(t) & y_a(t) \end{bmatrix}, \quad \boldsymbol{p}_k^o = \begin{bmatrix} x_k^o & y_k^o \end{bmatrix}^{\cdot}, \quad k = 1,2,\ldots,N_o. \tag{2}$$

where N_o is the number of static obstacles.

The inter-vehicle distance and the vehicle-obstacle distance are defined as

$$d_{ij}(\boldsymbol{q}) = \left\| \boldsymbol{p}_i - \boldsymbol{p}_j \right\|, \quad i, j = 1,2,\ldots,N_v,\ j \neq i, \qquad d_{ik}^o(\boldsymbol{q}) = \left\| \boldsymbol{p}_i - \boldsymbol{p}_k^o \right\|, \quad k = 1,2,\ldots,N_o. \tag{3}$$

The vehicle interaction bounds, the obstacle-repulsion activation interval, and the geometric safety relations are specified as

$$\underline{d} < d_{ij}(\boldsymbol{q}) < \bar{d}, \quad \underline{d}_o < d_{ik}^o(\boldsymbol{q}) < \bar{d}_o, \qquad R_v = \frac{1}{2}\sqrt{L_v^2 + W_v^2}, 2R_v < \underline{d}, R_v + R_o < \underline{d}_o. \tag{4}$$

where $\underline{d}$ and $\bar{d}$ are the lower and upper inter-vehicle distance bounds, while $\underline{d}_o$ and $\bar{d}_o$ denote the minimum obstacle-clearance distance and repulsion activation radius. L_v, W_v, R_v, R_o and denote the vehicle dimensions and corresponding envelope and obstacle radii.

For vehicle i, the APF-based guidance vector is constructed as

$$\boldsymbol{f}_i = \boldsymbol{f}_i^a + \boldsymbol{f}_i^v + \boldsymbol{f}_i^o = \begin{bmatrix} f_i^x \\ f_i^y \end{bmatrix}. \tag{5}$$

The vector $\boldsymbol{f}_i$ combines attraction guidance, inter-vehicle avoidance guidance, and obstacle-repulsion guidance. The terms $\boldsymbol{f}_i^a$, $\boldsymbol{f}_i^v$, and $\boldsymbol{f}_i^o$ denote the corresponding guidance components, respectively.

The attraction guidance vector is defined as

$$\boldsymbol{f}_i^a = k^a\left(\boldsymbol{p}_a - \boldsymbol{p}_i\right), \quad k^a > 0. \tag{6}$$

where k^a is the positive attraction gain.

The positive projection operator is defined as

$$[s]_+ = \max\{s, 0\}. \tag{7}$$

which activates the corresponding repulsive or cohesive guidance term according to the distance condition.

The inter-vehicle avoidance guidance vector and the obstacle-repulsion guidance vector are designed as

$$\begin{aligned} \boldsymbol{f}_i^v &= \sum_{\substack{j=1 \\ j\neq i}}^{N_v} \Bigg\{ \frac{\underline{k}^v}{d_{ij}\left(d_{ij} - \underline{d}\right)^2} \left[\frac{1}{d_{ij} - \underline{d}} - \frac{1}{\bar{d} - \underline{d}} \right]_+ \\ &\quad - \frac{\bar{k}^v}{d_{ij}} \left[d_{ij} - \bar{d} \right]_+ \Bigg\} \left(\boldsymbol{p}_i - \boldsymbol{p}_j \right), \\ \boldsymbol{f}_i^o &= \sum_{k=1}^{N_o} \frac{k^o}{d_{ik}^o\left(d_{ik}^o - \underline{d}_o\right)^2} \left[\frac{1}{d_{ik}^o - \underline{d}_o} - \frac{1}{\bar{d}_o - \underline{d}_o} \right]_+ \\ &\quad \times \left(\boldsymbol{p}_i - \boldsymbol{p}_k^o \right). \end{aligned} \tag{8}$$

where $\underline{k}^v > 0$ and $\bar{k}^v > 0$ are the positive gains associated with the lower-bound and upper-bound inter-vehicle distance terms, respectively, and $k^o > 0$ is the positive obstacle repulsion gain. The lower-bound inter-vehicle term is used for collision avoidance, the upper-bound inter-vehicle term is used for formation cohesion, and the obstacle-repulsion term is used for obstacle avoidance.

Based on the APF-based guidance vector, the desired guidance direction of vehicle i is defined as

$$\psi_i^a = \operatorname{atan2}\left(f_i^y, f_i^x\right). \tag{9}$$

where ψ_i^a is the APF-induced desired heading angle.

To align the vehicle heading with the APF-induced desired direction, the desired heading-rate constraint is prescribed as

$$\dot{\psi}_i = -\lambda_a\left(\psi_i - \psi_i^a\right), \qquad \lambda_a > 0. \tag{10}$$

where λ_a is the positive heading convergence gain. The heading error in Eq. (10) uses the shortest angular difference in (-π, π].

The desired heading-rate constraint in Eq. (10) can be expressed in the standard first-order constraint form:

$$\boldsymbol{A}\dot{\boldsymbol{q}}_i = \boldsymbol{b}_i. \tag{11}$$

where

$$\boldsymbol{A} = \begin{bmatrix} 0 & 0 & 1 \end{bmatrix}, \boldsymbol{b}_i = -\lambda_a\left(\psi_i - \psi_i^a\right). \tag{12}$$

Here, $\boldsymbol{A}$ selects the heading-rate component from $\dot{\boldsymbol{q}}_i$, and $\boldsymbol{b}_i$ represents the APF-induced desired heading-rate constraint.

3. Generalized Udwadia-Kalaba approach

The ICVs are indexed in a closed-chain order with adjacent pairs (1, 2), (2, 3), ..., $(N_v - 1, N_v)$, and $(N_v, 1)$; the entries of the adjacent-distance vector $\boldsymbol{d}^v(\boldsymbol{q})$ follow the same order.

The adjacent-pair distance constraints are reformulated as bounded error constraints. Based on the adjacent-pair distance vector $\boldsymbol{d}^v(\boldsymbol{q})$, the distance error vector is defined as

$$\boldsymbol{e}_v(\boldsymbol{q},t)=\boldsymbol{d}^v(\boldsymbol{q})-\boldsymbol{d}_f(t). \tag{13}$$

where $\boldsymbol{d}_f(t)\in\mathbb{R}^{N_v}$ denotes the corresponding reference distance vector.

The admissible bounds of the distance error vector are defined as

$$\underline{\boldsymbol{e}}_v<\boldsymbol{e}_v(\boldsymbol{q},t)<\bar{\boldsymbol{e}}_v,\qquad \underline{\boldsymbol{e}}_v+\bar{\boldsymbol{e}}_v=\boldsymbol{0}. \tag{14}$$

where the vector inequalities are understood componentwise.

The diffeomorphic mapping satisfies

$$\begin{cases}\lim\limits_{\boldsymbol{e}_v(\boldsymbol{q},t)\to\underline{\boldsymbol{e}}_v^+}\xi(\boldsymbol{q},t)=-\infty,\\ \lim\limits_{\boldsymbol{e}_v(\boldsymbol{q},t)\to\bar{\boldsymbol{e}}_v^-}\xi(\boldsymbol{q},t)=+\infty.\end{cases} \tag{15}$$

The normalized error vector is defined as

$$\boldsymbol{\eta}(\boldsymbol{q},t)=\frac{2\boldsymbol{e}_v(\boldsymbol{q},t)-\bar{\boldsymbol{e}}_v-\underline{\boldsymbol{e}}_v}{\bar{\boldsymbol{e}}_v-\underline{\boldsymbol{e}}_v}=\frac{\boldsymbol{e}_v(\boldsymbol{q},t)}{\bar{\boldsymbol{e}}_v}. \tag{16}$$

When $\boldsymbol{e}_v(\boldsymbol{q},t)\in(\underline{\boldsymbol{e}}_v,\bar{\boldsymbol{e}}_v)$, one has $\boldsymbol{\eta}(\boldsymbol{q},t)\in(-1,1)$. The transformed error vector is defined as

$$\begin{aligned}\xi(\boldsymbol{q},t)&=\operatorname{arctanh}(\boldsymbol{\eta}(\boldsymbol{q},t))=\frac{1}{2}\ln\left(\frac{1+\boldsymbol{\eta}(\boldsymbol{q},t)}{1-\boldsymbol{\eta}(\boldsymbol{q},t)}\right)\\&=\frac{1}{2}\ln\left(\frac{\boldsymbol{e}_v(\boldsymbol{q},t)+\bar{\boldsymbol{e}}_v}{\bar{\boldsymbol{e}}_v-\boldsymbol{e}_v(\boldsymbol{q},t)}\right).\end{aligned} \tag{17}$$

The desired transformed error dynamics is assigned as

$$\ddot{\xi}+\boldsymbol{K}_d\dot{\xi}+\boldsymbol{K}_p\xi=0,\qquad \boldsymbol{K}_p>0,\boldsymbol{K}_d>0. \tag{18}$$

where $\boldsymbol{K}_p$ and $\boldsymbol{K}_d$ are positive definite gain matrices for the transformed error dynamics.

Remark: With positive gains $\boldsymbol{K}_p$ and $\boldsymbol{K}_d$, Eq. (18) yields

$$\lim_{t\to+\infty}\xi(t)=\boldsymbol{0}. \tag{19}$$

According to the inverse diffeomorphic mapping in Eq. (17), the inter-vehicle distance asymptotically approaches $\boldsymbol{d}_f(t)$.

$$\boldsymbol{e}_v(t)=\frac{\bar{\boldsymbol{e}}_v+\underline{\boldsymbol{e}}_v}{2}+\frac{\bar{\boldsymbol{e}}_v-\underline{\boldsymbol{e}}_v}{2}\tanh(\xi(t)). \tag{20}$$

It follows from Eq. (13), Eq. (14), and Eq. (17) that

$$\lim_{t\to+\infty}\boldsymbol{e}_v(\boldsymbol{q},t)=0\Rightarrow\lim_{t\to+\infty}\boldsymbol{d}^v(\boldsymbol{q})=\boldsymbol{d}_f(t). \tag{21}$$

4. Control design and stability analysis

This section presents the constraint-following control design, including the nominal GUK-based control, the adaptive robust compensation, and the closed-loop stability analysis. The overall control input is designed as

$$\boldsymbol{\tau}=\boldsymbol{\tau}_g+\boldsymbol{\tau}_s+\boldsymbol{\tau}_r. \tag{22}$$

4.1. GUK-based adaptive robust control

Based on the Lagrangian formulation, the dynamics of the ICV are described by

$$\boldsymbol{M}(\boldsymbol{q},\boldsymbol{\sigma},t)\ddot{\boldsymbol{q}}+\boldsymbol{C}(\boldsymbol{q},\dot{\boldsymbol{q}},\boldsymbol{\sigma},t)\dot{\boldsymbol{q}}=\boldsymbol{\tau}. \tag{23}$$

Differentiating Eq. (11) gives

$$\boldsymbol{A}\ddot{\boldsymbol{q}}=\boldsymbol{b}_a,\qquad \boldsymbol{b}_a=\dot{\boldsymbol{b}}-\dot{\boldsymbol{A}}\dot{\boldsymbol{q}}. \tag{24}$$

Here, $\boldsymbol{b}_a$ denotes the acceleration-level constraint term obtained from the time derivative of the velocity-level constraint.

Based on Eq. (11), Eq. (23) and Eq. (24), the nominal acceleration can be derived as

$$\ddot{\boldsymbol{q}}=\boldsymbol{\Gamma}+\boldsymbol{\chi\mu}. \tag{25}$$

where

$$\begin{aligned}&\boldsymbol{\Gamma}=\overline{\boldsymbol{M}}^{-1/2}\left(\boldsymbol{A}\overline{\boldsymbol{M}}^{-1/2}\right)^{+}(\boldsymbol{b}_a+\boldsymbol{A}\overline{\boldsymbol{M}}^{-1}\overline{\boldsymbol{C}}\dot{\boldsymbol{q}})\\&-\overline{\boldsymbol{M}}^{-1}\overline{\boldsymbol{C}}\dot{\boldsymbol{q}},\\&\boldsymbol{\chi}=\boldsymbol{I}-\boldsymbol{A}^{+}\boldsymbol{A}=\begin{bmatrix}1&0&0\\0&1&0\\0&0&0\end{bmatrix}.\end{aligned} \tag{26}$$

Here, $\boldsymbol{\Gamma}$ is the nominal constraint-following acceleration, $\boldsymbol{\chi\mu}$ is the auxiliary acceleration term, and $(\cdot)^{+}$ denotes the Moore–Penrose pseudoinverse.

Differentiating Eq. (17) gives

$$\dot{\xi}=\frac{\partial\xi}{\partial\boldsymbol{q}}\dot{\boldsymbol{q}}+\frac{\partial\xi}{\partial t}. \tag{27}$$

Differentiating Eq. (27) and substituting Eq. (25) yields

$$\begin{aligned}\ddot{\xi}&=\frac{d}{dt}\left(\frac{\partial\xi}{\partial q}\right)\dot{\boldsymbol{q}}+\frac{\partial\xi}{\partial q}\ddot{\boldsymbol{q}}+\frac{d}{dt}\left(\frac{\partial\xi}{\partial t}\right)\\&=\frac{d}{dt}\left(\frac{\partial\xi}{\partial q}\right)\dot{\boldsymbol{q}}+\frac{\partial\xi}{\partial q}(\boldsymbol{\Gamma}+\boldsymbol{\chi\mu})+\frac{d}{dt}\left(\frac{\partial\xi}{\partial t}\right)\\&=\frac{\partial\xi}{\partial\boldsymbol{q}}\boldsymbol{\Gamma}+\frac{d}{dt}\left(\frac{\partial\xi}{\partial\boldsymbol{q}}\right)\dot{\boldsymbol{q}}+\frac{d}{dt}\left(\frac{\partial\xi}{\partial t}\right)+\frac{\partial\xi}{\partial\boldsymbol{q}}\boldsymbol{\chi\mu}\\&=\boldsymbol{h}_1(\boldsymbol{q},\dot{\boldsymbol{q}},t)+\boldsymbol{h}_2(\boldsymbol{q},\dot{\boldsymbol{q}},t)\boldsymbol{\mu}\end{aligned} \tag{28}$$

Here, $\boldsymbol{h}_1$ represents the drift term of the transformed constraint dynamics, and $\boldsymbol{h}_2$ maps the auxiliary input $\boldsymbol{\mu}$ to the transformed acceleration $\ddot{\xi}$.

Assumption 1: For all admissible $(\boldsymbol{q},\dot{\boldsymbol{q}},t)$, let H_1 and H_2 denote the range space and null space of $\mathbf{h}_2$, respectively. The following feasibility conditions are satisfied:

$$\begin{cases}-\boldsymbol{h}_1-K_d\dot{\xi}-K_p\xi\in\mathrm{H}_1(\boldsymbol{q},\dot{\boldsymbol{q}},t),\\ \left(\boldsymbol{I}-\boldsymbol{h}_2^{+}\boldsymbol{h}_2\right)\boldsymbol{\nu}\in\mathrm{H}_2(\boldsymbol{q},\dot{\boldsymbol{q}},t).\end{cases} \tag{29}$$

Under Assumption 1, the auxiliary input is selected as

$$\boldsymbol{\mu}^* = \boldsymbol{h}_2^+\left(-\boldsymbol{h}_1 - K_d\,\dot{\boldsymbol{\xi}} - K_p\boldsymbol{\xi}\right) + \left(\boldsymbol{I} - \boldsymbol{h}_2^+\boldsymbol{h}_2\right)\boldsymbol{\nu}. \tag{30}$$

The first term enforces the desired transformed error dynamics, while the second term introduces a secondary objective without changing it. The null-space input $\boldsymbol{\nu}$ is designed as

$$\boldsymbol{\nu} = \left[-\lambda_a\left(\dot{\boldsymbol{x}} - \boldsymbol{f}^x\right) \quad -\lambda_a\left(\dot{\boldsymbol{y}} - \boldsymbol{f}^y\right) \quad \boldsymbol{0}\right]^{\bullet}. \tag{31}$$

Here, the null-space input drives the translational velocity components toward the APF-induced guidance vector without changing the heading constraint.

Substituting Eq. (25) derived from Eq. (23) into the nominal dynamics gives

$$\begin{aligned}\boldsymbol{\tau}_g &= \overline{\boldsymbol{M}}\ddot{\boldsymbol{q}} + \overline{\boldsymbol{C}}\dot{\boldsymbol{q}} = \overline{\boldsymbol{M}}(\boldsymbol{\Gamma} + \chi\boldsymbol{\mu}^*) + \overline{\boldsymbol{C}}\dot{\boldsymbol{q}} \\ &= (\overline{\boldsymbol{M}}\boldsymbol{\Gamma} + \overline{\boldsymbol{C}}\dot{\boldsymbol{q}}) + \overline{\boldsymbol{M}}\chi\boldsymbol{\mu}^* = \boldsymbol{\tau}_{g_1} + \boldsymbol{\tau}_{g_2} \\ &= \overline{\boldsymbol{M}}^{1/2}\left(\boldsymbol{A}\overline{\boldsymbol{M}}^{-1/2}\right)^+(\boldsymbol{b}_a + \boldsymbol{A}\overline{\boldsymbol{M}}^{-1}\overline{\boldsymbol{C}}\dot{\boldsymbol{q}}) \\ &\quad + \overline{\boldsymbol{M}}\chi\boldsymbol{\mu}^*.\end{aligned} \tag{32}$$

Here, $\boldsymbol{\tau}_{g_1}$ is the nominal constraint-following term, and $\boldsymbol{\tau}_{g_2}$ is the nominal auxiliary transformed-constraint term.

The combined velocity-level constraint error is defined according to Eq. (11) as

$$\boldsymbol{\beta}(\boldsymbol{q},\dot{\boldsymbol{q}},t) = \boldsymbol{A}(\boldsymbol{q},t)\dot{\boldsymbol{q}} - \boldsymbol{b}(\boldsymbol{q},t). \tag{33}$$

Here, $\boldsymbol{\beta}$ denotes the velocity-level constraint error associated with the APF-induced guidance constraint. The stabilizing control term is

$$\boldsymbol{\tau}_s = -k_\beta\overline{\boldsymbol{M}}\boldsymbol{A}^{\text{晦}}\left(\boldsymbol{A}\boldsymbol{A}\ \ \right)^{-1}\boldsymbol{P}^{-1}\boldsymbol{\beta}, k_\beta > 0, \boldsymbol{P} > 0. \tag{34}$$

Here, $\boldsymbol{P}$ is a positive definite weighting matrix, and k_β is a feedback gain for suppressing the constraint error. Based on the ICV dynamics established in Eq. (23), the aggregate dynamic matrices of the multi-vehicle system are decomposed into nominal and uncertain components as

$$\begin{cases}\boldsymbol{M}(\boldsymbol{q},\boldsymbol{\sigma},t) = \overline{\boldsymbol{M}}(\boldsymbol{q}) + \Delta\boldsymbol{M}(\boldsymbol{q},\boldsymbol{\sigma},t), \\ \boldsymbol{C}(\boldsymbol{q},\dot{\boldsymbol{q}},\boldsymbol{\sigma},t) = \overline{\boldsymbol{C}}(\boldsymbol{q},\dot{\boldsymbol{q}}) + \Delta C(\boldsymbol{q},\dot{\boldsymbol{q}},\boldsymbol{\sigma},t).\end{cases} \tag{35}$$

where $\boldsymbol{M}$ and $\boldsymbol{C}$ denote the nominal inertia matrix and Coriolis–centrifugal matrix, respectively, while $\Delta\boldsymbol{M}$ and ΔC are their corresponding uncertain parts. The uncertain parameter vector $\boldsymbol{\sigma}$ belongs to an unknown compact set $\boldsymbol{\Sigma}$, and the uncertainties are bounded with unknown bounds. Here, t accounts for time-varying model uncertainty.

The auxiliary matrices are defined as

$$\begin{cases}\boldsymbol{D}(\boldsymbol{q}) = \overline{\boldsymbol{M}}^{-1}(\boldsymbol{q}), \\ \Delta\boldsymbol{D}(\boldsymbol{q},\boldsymbol{\sigma},t) = \boldsymbol{M}^{-1}(\boldsymbol{q},\boldsymbol{\sigma},t) - \overline{\boldsymbol{M}}^{-1}(\boldsymbol{q}), \\ \boldsymbol{E}(\boldsymbol{q},\boldsymbol{\sigma},t) = \overline{\boldsymbol{M}}(\boldsymbol{q})\boldsymbol{M}^{-1}(\boldsymbol{q},\boldsymbol{\sigma},t) - \boldsymbol{I}.\end{cases} \tag{36}$$

Here, $\boldsymbol{D}$, $\Delta\boldsymbol{D}$, and $\boldsymbol{E}$ are introduced to characterize the inverse-inertia mismatch caused by dynamic uncertainties.

Assumption 2: For a given positive definite matrix $\boldsymbol{P}$, define

$$\boldsymbol{\Xi}(\boldsymbol{q},\boldsymbol{\sigma},t) = \boldsymbol{PADE}\overline{\boldsymbol{M}}\boldsymbol{A}^{\text{晦}}\left(\boldsymbol{A}\boldsymbol{A}\ \ \right)^{-1}\boldsymbol{P}^{-1}. \tag{37}$$

There exists a constant $\lambda_E > -1$ such that

$$\frac{1}{2}\min_{\sigma\in\Sigma}\lambda_{\min}\left(\boldsymbol{\Xi}(\boldsymbol{q},\boldsymbol{\sigma},t) + \boldsymbol{\Xi}^{\bullet}(\boldsymbol{q},\boldsymbol{\sigma},t)\right) \geq \lambda_E. \tag{38}$$

Assumption 3: For the given positive definite matrix $\boldsymbol{P}$, there exists an unknown positive constant vector α and a known continuous bounding function $\Pi(\alpha,\boldsymbol{q},\dot{\boldsymbol{q}},t)$ such that for all $(\square,\boldsymbol{q},\dot{\boldsymbol{q}},t)$ and all $\boldsymbol{\sigma}\in\boldsymbol{\Sigma}$,

$$\begin{aligned}&\max_{\sigma\in\Sigma}\left\|\boldsymbol{PA}\Delta\boldsymbol{D}\left(-\overline{\boldsymbol{C}}\dot{\boldsymbol{q}} + \boldsymbol{\tau}_g + \boldsymbol{\tau}_s\right) - \boldsymbol{PAD}\Delta\boldsymbol{C}\dot{\boldsymbol{q}}\right\| \\ &\leq (1+\lambda_E)\Pi(\alpha,\boldsymbol{q},\dot{\boldsymbol{q}},t).\end{aligned} \tag{39}$$

Assumption 4: The uncertainty bound function is linearly parameterizable. There exists a known continuous basis function vector $\Pi(\boldsymbol{q},\dot{\boldsymbol{q}},t)$ such that

$$\begin{aligned}\Pi(\boldsymbol{\alpha},\boldsymbol{q},\dot{\boldsymbol{q}},t) &= \boldsymbol{\alpha}_{\dot q^2}\left\|\dot{\boldsymbol{q}}\right\|^2 + \boldsymbol{\alpha}_{\dot q}\left\|\dot{\boldsymbol{q}}\right\| + \boldsymbol{\alpha}_c \\ &\leq \max\left\{\boldsymbol{\alpha}_{\dot q^2}, \frac{\boldsymbol{\alpha}_{\dot q}}{2}, \boldsymbol{\alpha}_c\right\}\left(\left\|\dot{\boldsymbol{q}}\right\| + 1\right)^2 \\ &= \alpha^{\bullet}\,\Pi(\boldsymbol{q},\dot{\boldsymbol{q}},t).\end{aligned} \tag{40}$$

The function $\Pi(\square,\boldsymbol{q},\dot{\boldsymbol{q}},t)$ is linear and non-decreasing with respect to $\boldsymbol{\alpha}$.

The sinusoidal adjustment factor is defined as

$$\omega\left(\left\|\boldsymbol{\Pi}\right\|\right) = \begin{cases}1, & \left\|\boldsymbol{\Pi}\right\| \geq \varepsilon_\omega, \\ \sin\left(\dfrac{\left\|\boldsymbol{\Pi}\right\|}{\varepsilon_\omega}\cdot\dfrac{\pi}{2}\right), & \left\|\boldsymbol{\Pi}\right\| < \varepsilon_\omega.\end{cases} \tag{41}$$

This factor smooths the robust compensation near zero.

The adaptive update law is

$$\dot{\alpha} = k_1\Pi\omega\left(\left\|\Pi\right\|\right)\left\|\boldsymbol{\beta}\right\| - k_2\alpha. \tag{42}$$

where $k_1 > 0$ is the adaptive gain, $k_2 > 0$ is the leakage coefficient, and $\boldsymbol{\alpha}(t_0) > 0$ componentwise.

The adaptive robust compensation term is

$$\boldsymbol{\tau}_r = -\overline{\boldsymbol{M}}\boldsymbol{A}^{\text{晦}}\left(\boldsymbol{A}\boldsymbol{A}\ \ \right)^{-1}\boldsymbol{P}^{-1}\boldsymbol{\beta}\omega\left(\left\|\Pi\right\|\right)\left(\alpha^{\bullet}\,\Pi\right)^2. \tag{43}$$

The implementation of the proposed framework is shown in Fig. 3 and summarized as follows:

- The diffeomorphic barrier transformation converts bounded formation safety constraints into unconstrained error variables and introduces the auxiliary boundary-related term.
- The constraint formulation leads to velocity- and acceleration-level constraint equations, from which the nominal constraint-following term is derived for nominal control design.
- Stabilizing and adaptive robust terms are designed based on constraint errors to regulate the ICV Lagrangian dynamics under uncertainties.

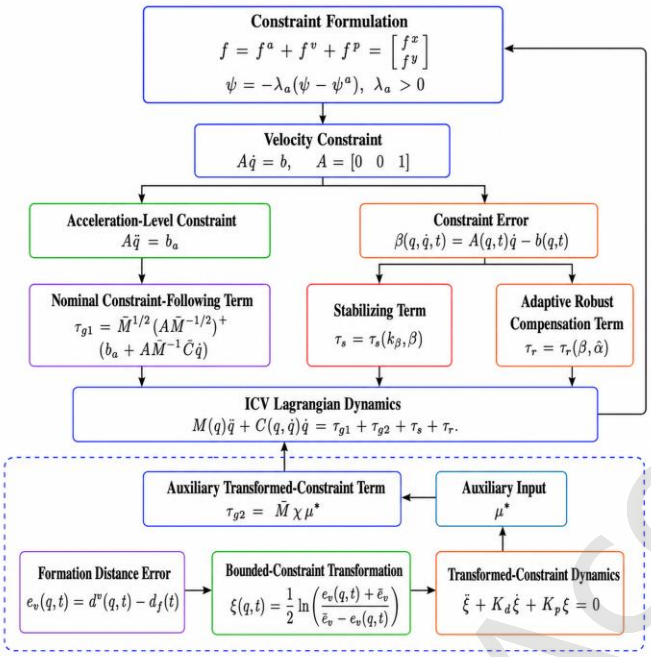

Fig. 3. Hierarchical control and optimization flow chart.

4.2. Closed-loop stability analysis

Theorem: Consider the constrained multi-vehicle system under Assumptions 1–4. With the adaptive law in Eq. (42), the control input in Eq. (22), and suitable control gains, the closed-loop system has the following properties:

1. Uniform boundedness: For any initial bound $r_0 > 0$, there exists $L(r_0) < \infty$ such that $\| \boldsymbol{z}(t_0)\| \le r_0$ implies $\| \boldsymbol{z}(t)\| \le L(r_0)$ for all $t \ge t_0$.

2. Uniform ultimate boundedness: For any $\| \boldsymbol{z}(t_0)\| \le r_0$, there exists $\underline{r} > 0$ such that, for any $\overline{r} > \underline{r}$, there exists a finite time $T(\overline{r}, r_0)$. for which $\| \boldsymbol{z}(t)\| \le \overline{r}$ holds for all $t \ge t_0 + T(\overline{r}, r_0)$.

Proof. Define the transformed constraint state as

$$\boldsymbol{\zeta} = \begin{bmatrix} \xi^{\cdot} & \dot{\xi}^{\cdot} \end{bmatrix}^{\cdot} \in \square^{2N_v}. \tag{44}$$

Define the uncertainty bound estimation error and the augmented error vector as

$$e_\alpha = \alpha - \alpha, \quad \boldsymbol{z} = \begin{bmatrix} \boldsymbol{\beta}^{晦} & e_\alpha & \boldsymbol{\zeta}^{?} \end{bmatrix}^{\cdot}. \tag{45}$$

From the transformed constraint dynamics assigned in Eq. (18), define

$$\boldsymbol{A}_\xi = \begin{bmatrix} 0 & \boldsymbol{I} \\ -\boldsymbol{K}_p & -\boldsymbol{K}_d \end{bmatrix}. \tag{46}$$

Choose $\boldsymbol{K}_p > 0$ and $\boldsymbol{K}_d > 0$ such that $\boldsymbol{A}_\xi$ is Hurwitz. Then, for any $\boldsymbol{Q}_\xi > 0$, there exists a positive definite matrix $\boldsymbol{R}_\xi$ satisfying

$$\boldsymbol{A}_\xi^{\cdot}\boldsymbol{R}_\xi + \boldsymbol{R}_\xi\boldsymbol{A}_\xi = -\boldsymbol{Q}_\xi. \tag{47}$$

Choose the Lyapunov candidate as

$$\boldsymbol{V} = \boldsymbol{\beta}^{晦}\boldsymbol{P}\boldsymbol{\beta} + \frac{1+\lambda_E}{k_1} e_\alpha e_\alpha + \lambda_\xi \boldsymbol{\zeta}^{?}\boldsymbol{R}_\xi\boldsymbol{\zeta} \ge 0. \tag{48}$$

where $\lambda_\xi > 0$, $\boldsymbol{P} > 0$, and $\boldsymbol{R}_\xi > 0$.

By Assumption 4, $\boldsymbol{\Pi}(\boldsymbol{q}, \dot{\boldsymbol{q}}, t)$ is continuous. On any compact admissible set considered in the analysis, it is bounded as

$$\exists \gamma > 0, \quad \left\| \boldsymbol{\Pi}(\boldsymbol{q}, \dot{\boldsymbol{q}}, t) \right\| \le \gamma. \tag{49}$$

Differentiating $\boldsymbol{V}$ along the closed-loop trajectories and using Eq. (18), Eq. (44), Eq. (22), Eq. (47), and Assumptions 2–4, and then applying Young's inequality (Chen, 1996; Chen and Zhang, 2010), yields the following inequality:

$$\begin{aligned} \dot{\boldsymbol{V}} \le & -\left[2k_\beta - \gamma(1+\lambda_E)\right]\| \boldsymbol{\beta}\|^2 \\ & -\left[\frac{(1+\lambda_E)k_2}{k_1} - \gamma(1+\lambda_E)\right]\| e_\alpha\|^2 \\ & -\lambda_\xi\lambda_{\min}\left(\boldsymbol{Q}_\xi\right)\| \zeta\|^2 + 2\gamma(1+\lambda_E)\| \alpha\| \ \| \boldsymbol{\beta}\| \\ & + \frac{(1+\lambda_E)k_2}{k_1}\| \alpha\|^2 + \frac{\varepsilon_\omega}{2}. \end{aligned} \tag{50}$$

Moreover, from Eq. (45) one has

$$\begin{aligned} & \| \boldsymbol{z}\|^2 = \| \boldsymbol{\beta}\|^2 + \| e_\alpha\|^2 + \| \boldsymbol{\zeta}\|^2 \\ & \| \boldsymbol{\beta}\| \le \| \boldsymbol{z}\|, \quad \| e_\alpha\| \le \| \boldsymbol{z}\|, \quad \| \boldsymbol{\zeta}\| \le \| \boldsymbol{z}\|. \end{aligned} \tag{51}$$

Therefore, Eq. (50) can be upper bounded by

$$\dot{\boldsymbol{V}} \le -\tilde{n}_1\| \boldsymbol{z}\|^2 + \tilde{n}_2\| \boldsymbol{z}\| + \tilde{n}_3, \tag{52}$$

where

$$\begin{aligned} & \tilde{n}_1 = \min\left\{2k_\beta - \gamma(1+\lambda_E), \lambda_\xi\lambda_{\min}\left(\boldsymbol{Q}_\xi\right), \right. \\ & \left. \frac{(1+\lambda_E)k_2}{k_1} - \gamma(1+\lambda_E)\right\} > 0, \\ & \tilde{n}_2 = 2\gamma(1+\lambda_E)\| \boldsymbol{\alpha}\|, \\ & \tilde{n}_3 = \frac{(1+\lambda_E)k_2}{k_1}\| \boldsymbol{\alpha}\|^2 + \frac{\varepsilon_\omega}{2}. \end{aligned} \tag{53}$$

From Eq. (48), there exist positive constants ϑ_1 and ϑ_2 such that

$$\vartheta_1 \|\boldsymbol{z}\|^2 \le \boldsymbol{V} \le \vartheta_2 \|\boldsymbol{z}\|^2, \tag{54}$$

where

$$\begin{cases} \vartheta_1 = \min\left\{ \lambda_{\min}\left(\boldsymbol{P}\right), \dfrac{1+\lambda_E}{k_1}, \lambda_\xi \lambda_{\min}\left(\mathrm{R}_\xi\right) \right\}, \\ \vartheta_2 = \max\left\{ \lambda_{\max}\left(\boldsymbol{P}\right), \dfrac{1+\lambda_E}{k_1}, \lambda_\xi \lambda_{\max}\left(\mathrm{R}_\xi\right) \right\}. \end{cases} \tag{55}$$

The critical radius associated with Eq. (52) is determined by

$$-\text{耨}_1 r_c^2 + \ _2 r_c + ?_3 = 0 \Rightarrow r_c = \frac{\text{耨}_2 + \sqrt{\ _2^2 + 4\text{耨}_1\ _3}}{2\tilde{n}_1}. \tag{56}$$

When $\|\boldsymbol{z}\| > r_c$, Eq. (52) gives $\dot{\boldsymbol{V}} < 0$. Then, for all $t \ge t_0$, the uniform boundedness property follows as

$$\|\boldsymbol{z}(t)\| \le \boldsymbol{L}(r_0) = \begin{cases} \sqrt{\dfrac{\vartheta_2}{\vartheta_1}} r_c, & r_0 \le r_c, \\ \sqrt{\dfrac{\vartheta_2}{\vartheta_1}} r_0, & r_0 > r_c. \end{cases} \tag{57}$$

For any $\bar{r} > \underline{r}$, define

$$\underline{r} = \sqrt{\frac{\vartheta_2}{\vartheta_1}} r_c, \delta = \text{耨}_1 \frac{\vartheta_1}{\vartheta_2} \bar{r}^2 - \ _2 \bar{r} \sqrt{\frac{\vartheta_1}{\vartheta_2}} - ?_3 > 0. \tag{58}$$

The corresponding convergence time can be selected as

$$T(\bar{r}, r_0) = \begin{cases} 0, & r_0 \le \bar{r}\sqrt{\dfrac{\vartheta_1}{\vartheta_2}}, \\ \dfrac{\vartheta_2 r_0^2 - \vartheta_1 \bar{r}^2}{\delta}, & r_0 > \bar{r}\sqrt{\dfrac{\vartheta_1}{\vartheta_2}}. \end{cases} \tag{59}$$

Thus the uniform ultimate boundedness property is obtained as

$$\|\boldsymbol{z}(t)\| \le \bar{r}, \quad t \ge t_0 + T(\bar{r}, r_0). \tag{60}$$

This completes the proof.

5. Simulation validation

This section presents the simulation settings and compares the proposed adaptive robust controller (ARC) with an LQR-based controller. The initial positions of the four ICVs are arranged clockwise as

$$\boldsymbol{P}_0 = \begin{bmatrix} 1.70 & 6.85 & 6.35 & 2.10 \\ 16.20 & 16.30 & 12.60 & 12.90 \end{bmatrix} m \tag{61}$$

The positions of the three circular obstacles and the obstacle radius are given by

$$\boldsymbol{P}^{\mathrm{o}} = \begin{bmatrix} 15 & 35 & 55 \\ 15 & 15 & 15 \end{bmatrix} \mathrm{m}, \qquad R_{\mathrm{o}} = 3.0\mathrm{m}. \tag{62}$$

The five points used to generate the quartic attractive trajectory are

$$\boldsymbol{P}^{\mathrm{a}} = \begin{bmatrix} 4.25 & 15 & 35 & 55 & 70 \\ 14.50 & 21 & 9 & 21 & 15 \end{bmatrix} \mathrm{m}. \tag{63}$$

The corresponding quartic attractive curve is expressed as

$$\begin{aligned} y_a(x) = &-3.6928 \times 10^{-5} x^4 + 5.3974 \times 10^{-3} x^3 \\ &-2.5054 \times 10^{-1} x^2 + 3.9443x + 1.8597. \end{aligned} \tag{64}$$

The attractive point $\boldsymbol{P}^{\mathrm{a}}$ in Eq. (2) moves along Eq. (64) at a constant arc-length speed.

For the dynamic modeling of the differential-drive ICV, the inertia matrix in Eq. (23) is

$$\boldsymbol{M}_i = \begin{bmatrix} m_i & 0 & m_i \ell_i \sin\psi_i \\ 0 & m_i & m_i \ell_i \cos\psi_i \\ m_i \ell_i \sin\psi_i & m_i \ell_i \cos\psi_i & \mathrm{I}_i \end{bmatrix}, \tag{65}$$

where m_i, I_i, and ℓ_i denote the mass, yaw moment of inertia, and distance from the center of mass to the rear axle of the i-th ICV, respectively.

The velocity-dependent term is given by

$$\boldsymbol{C}_i \dot{\boldsymbol{q}}_i = \begin{bmatrix} m_i \ell_i \dot{\psi}_i^2 \cos\psi_i - \sin\psi_i \Upsilon_i \\ m_i \ell_i \dot{\psi}_i^2 \sin\psi_i + \cos\psi_i \Upsilon_i \\ -\ell_i \Upsilon_i \end{bmatrix}, \tag{66}$$

where

$$\Upsilon_i = m_i \left(\dot{x}_i \cos\psi_i + \dot{y}_i \sin\psi_i \right) \dot{\psi}_i. \tag{67}$$

The generalized force $\boldsymbol{\tau}_i$ is obtained from the left- and right-wheel torques through the input mapping

$$\boldsymbol{\tau}_i = \boldsymbol{T}_i \boldsymbol{u}_i = \frac{1}{r_i} \begin{bmatrix} \cos\psi_i & \cos\psi_i \\ \sin\psi_i & \sin\psi_i \\ \ell_i^{\mathrm{w}} & -\ell_i^{\mathrm{w}} \end{bmatrix} \begin{bmatrix} u_i^L \\ u_i^R \end{bmatrix}, \tag{68}$$

where r_i is the wheel radius, ℓ_i^{w} is the lateral distance from each wheel to the vehicle centerline, and u_i^L and u_i^R are the left- and right-wheel torques, respectively.

The basic parameters of each ICV are listed in **Table 1**.

Table 1 Basic physical parameters of each ICV

Parameter	$\bar{m}_i$	$\bar{I}_i$	$\ell_i\,(\mathrm{m})$	$r_i\,(\mathrm{m})$	$\ell_i^{\mathrm{w}}\,(\mathrm{m})$
Value	50	12.5	0.30	0.08	0.35

To evaluate disturbance compensation, the vehicle mass and yaw moment of inertia are both varied periodically:

$$\begin{cases} m_i(t) = \bar{m}_i + 0.06\bar{m}_i \sin(2.0t), \\ \mathrm{I}_i(t) = \bar{\mathrm{I}}_i + 0.06\bar{\mathrm{I}}_i \sin(2.0t). \end{cases} \tag{69}$$

In addition, sinusoidal perturbations are applied to the four ICVs, as shown in **Table 2**.

Table 2 Sinusoidal disturbances on each ICV

ICV	Ω_{xi} (N)	Ω_{yi} (N)	$\Omega_{\psi i}$ (N·m)
1	2.0 sin t	1.5 cos t	0.40 sin t
2	1.6 cos t	2.0 sin t	0.35 cos t
3	2.2 sin t	1.8 cos t	0.45 sin t

4	1.8 cos t	2.4 sin t	0.50 cos t

For the LQR-based comparison, the adaptive robust compensation term in Eq. (22) is replaced by τ_L, defined as

$$\tau_L = -\kappa \bar{M}(q)\begin{bmatrix} 0 \\ 0 \\ K_L\left(\dot{\psi}-\dot{\psi}^a\right) \end{bmatrix}. \tag{70}$$

The APF and control parameters are listed in **Table 3**.

Table 3 APF and control parameters

APF parameters		Control parameters	
k^a	0.50	$\boldsymbol{P}$	1.0
k^o	3.0	$\boldsymbol{\alpha}(0)$	1. 0
λ_a	1.0	$(\varepsilon_\omega, k_\beta)$	(1.0,18)
$(\underline{d} \mid \bar{d})$	(2.0, 6.0) m	$(k_1 \mid k_2)$	(5.0, 0.02)
$(\underline{d}_o \mid \bar{d}_o)$	(4.0, 8.0) m	$(\boldsymbol{K}_p \mid \boldsymbol{K}_d)$	(12, 6)
$(\underline{k}^v \mid \bar{k}^v)$	(5.0, 0.40)	(κ, K_L)	(1, 0.15)

According to Eq. (13), the reference inter-vehicle distance is selected as

$$d_{f_1} = \frac{\bar{d}+\underline{d}}{2} = 4. \tag{71}$$

The trajectories in Fig. 4 show that the APF guidance and distance constraints enable both controllers to avoid inter-ICV and obstacle collisions while completing the prescribed path.

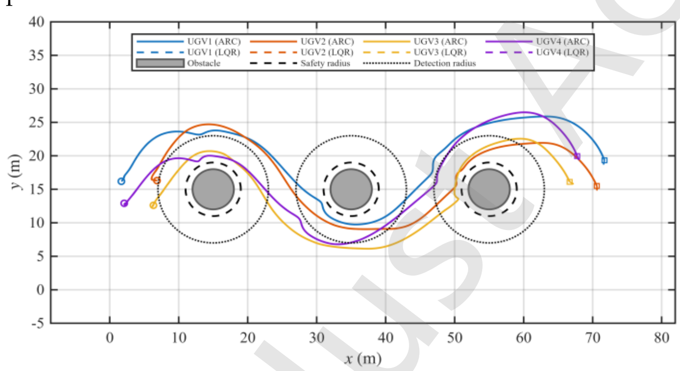

Fig. 4. Trajectory tracking and obstacle-avoidance results.

Fig. 5 shows the adjacent-vehicle distances. Initially, the APF-based inter-vehicle repulsion separates neighboring vehicles, while the GUK constraint regulates the spacing toward the prescribed desired value.

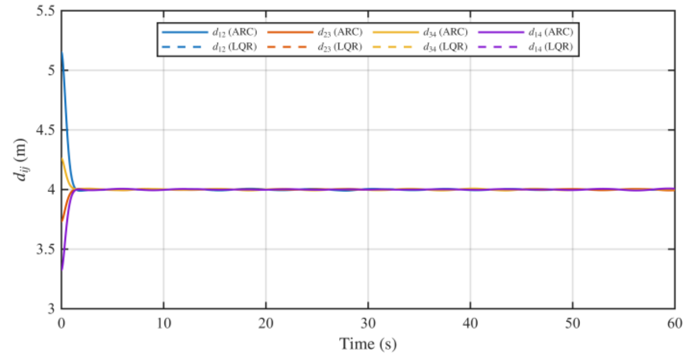

Fig. 5. Inter-ICV distance responses under ARC and LQR.

Fig. 6 shows the vehicle-obstacle distances and the number of activated obstacle-avoidance constraints. The obstacle repulsion is activated as vehicles enter the prescribed detection range and is released after they leave it.

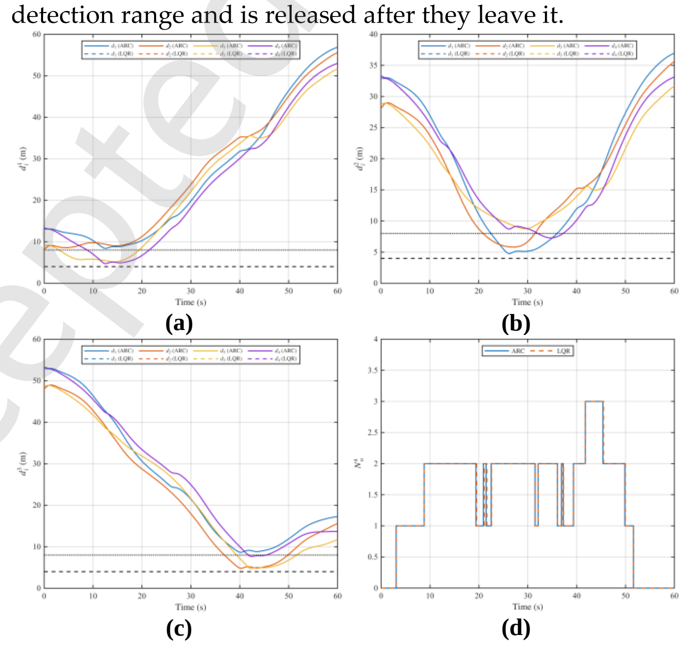

Fig. 6. Obstacle-distance responses and activation of the obstacle-avoidance constraints: (a) distances to obstacle 1; (b) distances to obstacle 2; (c) distances to obstacle 3; (d) number of ICVs within the obstacle-detection radius.

Fig. 7 shows the sliding-variable responses defined by Eq. (33). In ARC, an increase in $|\boldsymbol{\beta}|$ strengthens the adaptive update in Eq. (42), so the robust compensation is adjusted online when disturbances enlarge the constraint error, whereas the LQR controller has no corresponding adaptive update.

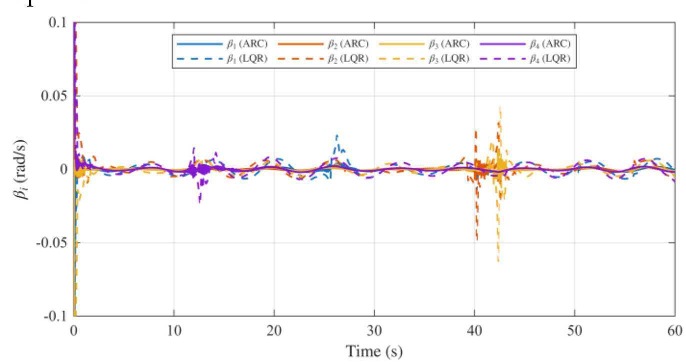

Fig. 7. Sliding-variable responses under ARC and LQR.

The accumulated constraint error of each ICV is quantified by

$$W_i^{\beta} = \int_0^T \left| \dot{\psi}_i(t) + \lambda_a \left[\psi_i(t) - \psi_i^a(t) \right] \right| \mathrm{d}t. \quad (72)$$

where W_i^{β} denotes the accumulated sliding-variable error of the i-th ICV over the simulation horizon.

Fig. 错误!未找到引用源。 compares W_i^{β} for the LQR controller and four ARC parameter settings; the quantitative results are summarized in **Table 4**. The reduction in W_i^{β} indicates that stronger adaptive settings enhance error-driven compensation.

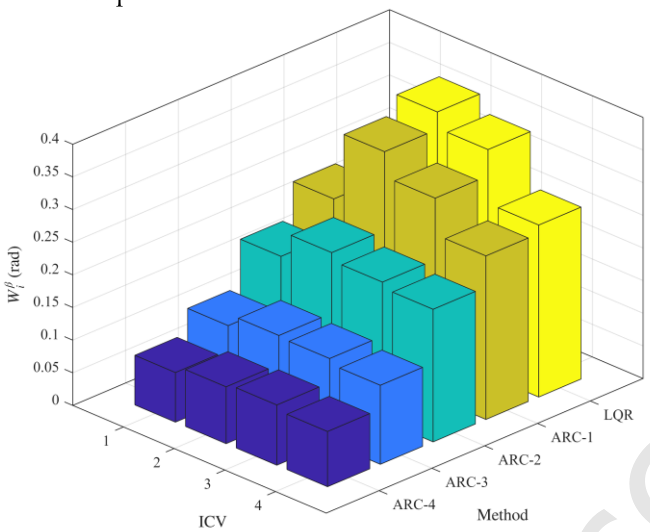

Fig. 8. Accumulated sliding-variable index for each ICV under ARC parameter variations and LQR.

Table 4 Comparison of the accumulated constraint-error index

Method	K_1	K_2	$\alpha(0)$	W_i^{β} (rad)	Reduction (%)
LQR	--	--	--	0.308125	--
ARC-1	0.02	0.45	0.05	0.284783	7.58
ARC-2	1.00	0.05	0.50	0.205893	33.18
ARC-3	2.00	0.02	0.80	0.123622	59.88
ARC-4	5.00	0.02	1.00	0.084882	72.45

For the distance-constraint parameter scan, K_p and K_d in the transformed-error dynamics in Eq. (18) are varied. The averaged formation-distance error index is defined as

$$\bar{W}_d(K_p, K_d) = \frac{1}{N_v T} \sum_{i=1}^{N_v} \int_0^T \left| d_i^v(t) - d_f(t) \right| \mathrm{d}t. \quad (73)$$

Fig. **9** shows the $\bar{W}_d$ over the $K_p - K_d$ grid; where lower values indicate smaller spacing errors.. K_p is scanned from 5 to 40 and K_d from 2 to 30 on a 6 × 6 grid. Each case is simulated for 60 s using ode15s with RelTol = 1e-5, AbsTol = 1e-7, and MaxStep = 0.05 s.

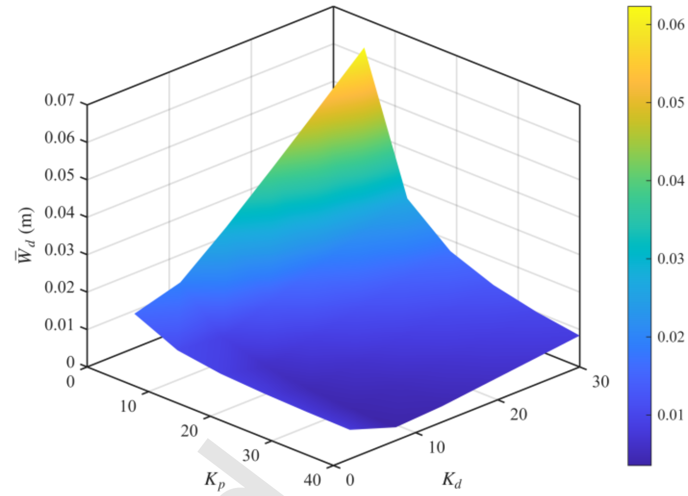

Fig. 9. Parameter-scan surface of the averaged formation-distance error index.

Fig. **10**, Fig. **11**, and Fig. **12** show the generalized control inputs in the x-, y-, and heading directions. In ARC, the adaptive robust term changes with $\boldsymbol{\beta}$ and the online estimate, so disturbance-induced constraint errors directly modify the total generalized force. LQR uses fixed-gain feedback and does not adaptively rescale this compensation.

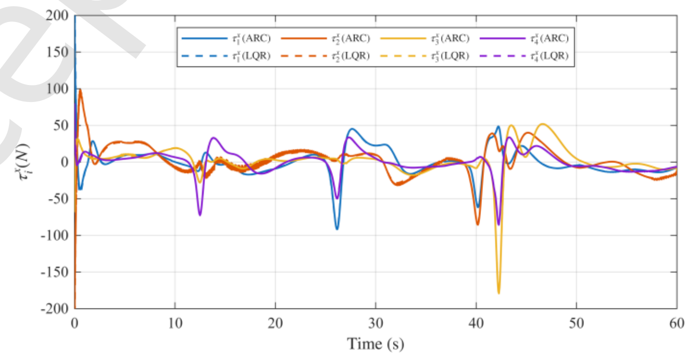

Fig. 10. Generalized control input in the x-direction.

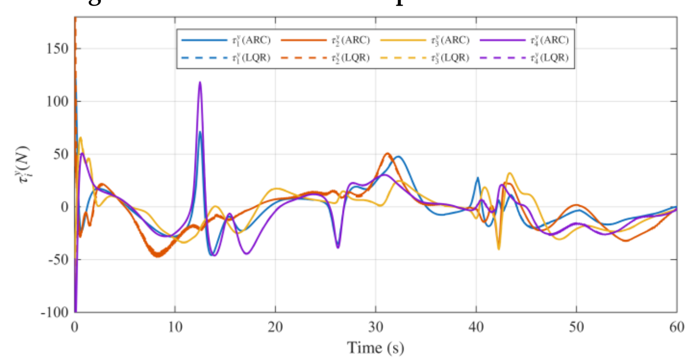

Fig. 11. Generalized control input in the y-direction.

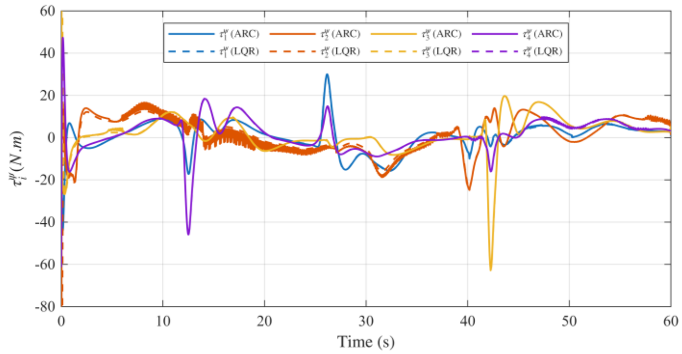

Fig. 12. Generalized control input in the heading direction.

Fig. **13** shows the wheel torques mapped by Eq. (68). Left- and right-wheel torque adjustments reflect ARC's online compensation for disturbances and parameter uncertainties.

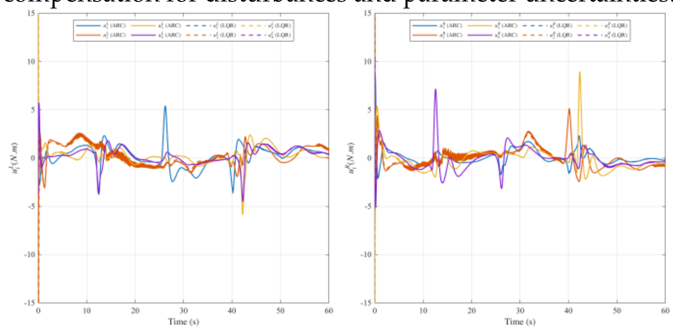

(a) (b)

Fig. 13. Mapped wheel torques of the ICVs: (a) left-wheel torques; (b) right-wheel torques.

Based on Eq. (5), Fig. **14** shows the x- and y-direction velocity responses during reference tracking, obstacle avoidance, and formation adjustment.

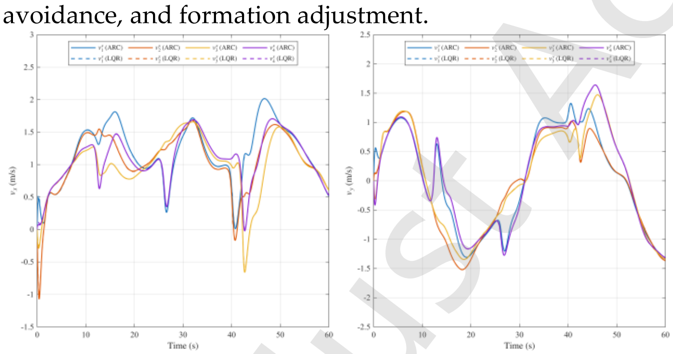

(a) (b)

Fig. 14. ICV velocity (a) x-direction; (b) y-direction.

According to Eq. (32), Fig. **15** and Fig. **16** show the x- and y-direction components of the transformed-constraint control term, which vary with adjacent-distance error to support formation deformation and spacing recovery.

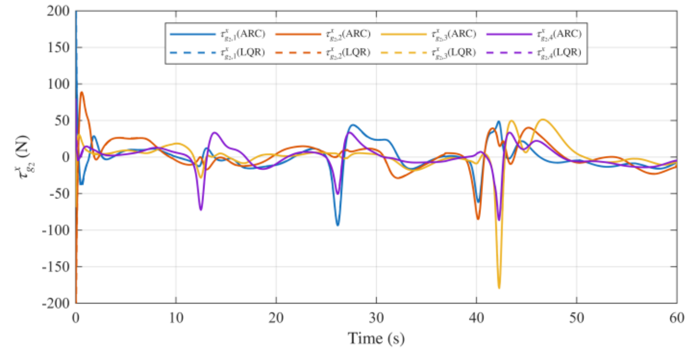

Fig. 15. Transformed-constraint control in the x-direction.

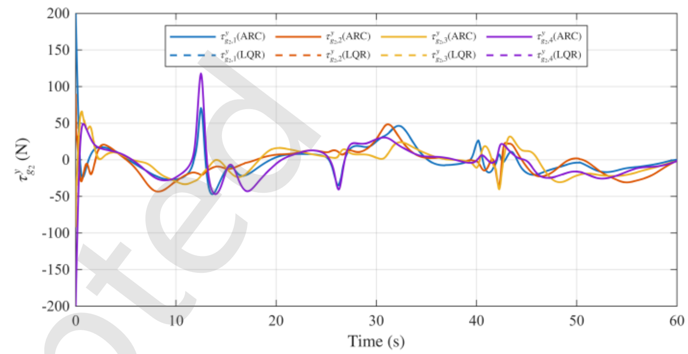

Fig. 16. Transformed-constraint control in the y-direction.

Fig. **17** shows the heading-direction component induced by planar-heading coupling in Eq. (65).

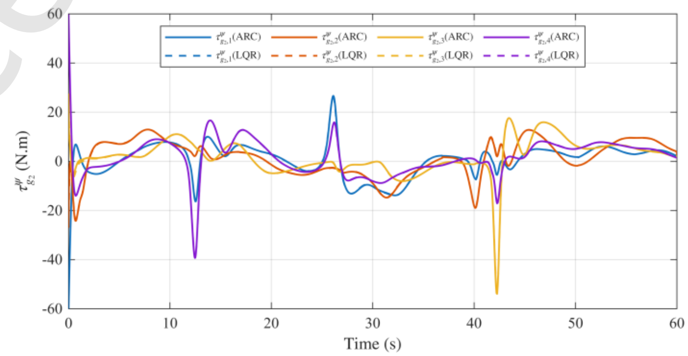

Fig. 17. Transformed-constraint control in the heading direction.

To examine the flexibility of the proposed GUK constraint controller under different spacing requirements, additional tests with time-varying spacing are conducted under nominal conditions. The parametric variations in Eq. (69), the disturbances in **Table 2**, the stabilizing term in Eq. (34), and the adaptive robust compensation term in Eq. (43) are excluded. Two representative time-varying desired-distance profiles are considered.

The first desired distance follows a cosine-type periodic law, defined as

$$d_{f_2}(t) = 4.0 + 1.5\cos\left(\frac{\pi}{10}t\right). \tag{74}$$

The cosine-type results are shown in Fig. **18**, where the adjacent-vehicle distances follow the periodic reference while the vehicles execute the corresponding formation adjustment.

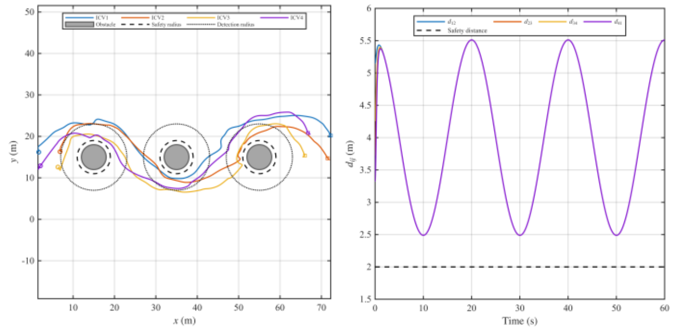

(a) (b)

Fig. 18. Responses for cosine-type time-varying formation spacing: (a) ICV trajectories; (b) adjacent-vehicle distances.

To further examine performance under monotonic spacing adjustment, the second desired distance follows an exponential decay law given by

$$d_{f_3}(t) = 3.0 + 2.5e^{-0.08t}. \quad (75)$$

Fig. 19 shows the exponential-spacing case, in which the adjacent-vehicle distances continuously adjust toward the prescribed final value.

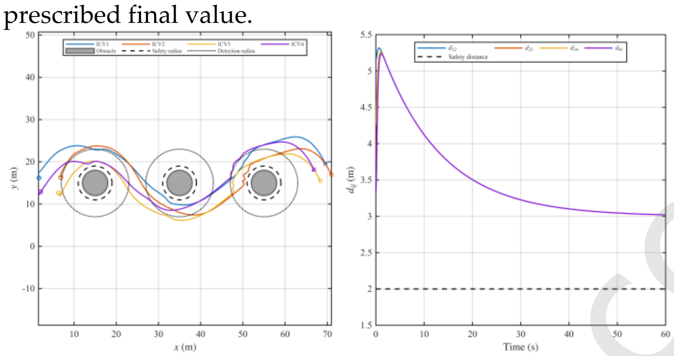

(a) (b)

Fig. 19. Responses for exponential-type time-varying formation spacing: (a) ICV trajectories; (b) adjacent-vehicle distances.

Together with the fixed-spacing case, these results demonstrate that the same GUK constraint-control structure can accommodate fixed, periodic, and monotonic spacing profiles.

6. Conclusion

This paper investigated the safe formation control problem for uncertain ICVS systems in obstacle-rich environments. A unified constraint-following formulation was established to describe inter-agent collision avoidance, obstacle evasion, formation deformation, and formation recovery within the same framework. Artificial potential field functions were used to characterize obstacle-avoidance and collision-avoidance requirements, while diffeomorphism-based transformed constraints were introduced to handle bounded distance constraints between adjacent ICVs. Based on the generalized Udwadia–Kalaba equation, the coupled safety and formation requirements were converted into a constraint-following control problem suitable for uncertain nonlinear swarm dynamics. An adaptive robust controller was then developed to compensate for model uncertainties, parameter perturbations, and external disturbances. Theoretical analysis proved the boundedness of the closed-loop signals. Simulation results, including the comparison between ARC and the LQR-based controller, verified obstacle evasion, collision prevention, formation maintenance, and spacing recovery. ARC also reduced the accumulated constraint error and adjusted the generalized control force and corresponding wheel torques online in response to disturbance-induced errors. These results demonstrate the effectiveness of the proposed constraint-oriented framework for safe and robust ICVS formation control in obstacle-rich environments. Future work will consider more practical scenarios, including communication delays, sensing uncertainties, dynamic obstacles, and experimental validation on physical ICVS platforms.

Author contributions

Xiaomin Zhao: Conceptualization, Methodology, Supervision, Funding acquisition, Writing – review & editing

Bingwen Wang: Methodology, Software, Formal analysis, Data curation, Writing – original draft

Xinhua Gao: Validation, Project administration, Writing – review & editing

Weilong Hu: Investigation, Data curation

Ye-Hwa Chen: Methodology, Supervision, Writing – review & editing

Replication and data sharing

The source data associated with this research are available from the corresponding author upon reasonable request.

Acknowledgements

This work was supported in part by the National Natural Science Foundation of China under Grant 52472404, the Natural Science Foundation of Anhui under Grant 2408085ME137, the Anhui Provincial Development and Reform Commission under Grant AHZDCYCXJH-QC2025-03, and the Key Science & Technology Project of Anhui Province under Grant 202523f12050013.

Declaration of competing interest

The authors declare no competing interests relevant to the content of this article.

References

Axelsson, J., 2017. Safety in vehicle platooning: a systematic literature review. IEEE Transactions on Intelligent Transportation Systems, 18, 1033–1045.

Cai, M., Xu, Q., Chen, C., Wang, J., Li, K., Wang, J., 2022. Multi-lane unsignalized intersection cooperation with flexible lane direction based on multi-vehicle formation control. IEEE Transactions on Vehicular Technology, 71, 5787–5798.

Chen, Y.-H., 1996. Performance analysis of controlled uncertain systems. Dynamics and Control, 6, 131–142.

Chen, Y.-H., 2008. Artificial swarm system: boundedness, convergence, and control. Journal of Aerospace Engineering, 21, 288–293.

Chen, Y.-H., Zhang, X., 2010. Adaptive robust approximate constraint-following control for mechanical systems. Journal of the Franklin Institute, 347, 69–86.

Chu, D., Zhao, C., Wang, R., Xiao, Q., Wang, W., Cao, D., 2024. A survey of multi-vehicle consensus in uncertain networks for autonomous driving. IEEE Transactions on Intelligent Transportation Systems, 25, 19319–19341.

Corless, M.J., Leitmann, G., 1981. Continuous state feedback guaranteeing uniform ultimate boundedness for uncertain dynamic systems. IEEE Transactions on Automatic Control, AC-26, 1139–1144.

Dong, P., Li, J., Guo, W., Zhang, H., Zhao, P., Xu, X., et al., 2025. Robust optimal path tracking control for intelligent vehicles equipped with wheel modules based on continuous integral sliding mode control. Automotive Innovation, 8, 385–404.

Dong, Q., Yan, Z., Nakano, K., Ji, X., Liu, Y., 2023. Graph-based scenario-adaptive lane-changing trajectory planning for autonomous driving. IEEE Robotics and Automation Letters, 8, 5688–5695.

Gao, Z., Hao, H., Gao, F., Zhao, R., 2025. Behavior-constrained multi-agent proximal policy optimization for cooperative vehicle control at future intersections. Automotive Innovation, 8, 896–912.

Hwang, C.-L., Abebe, H.B., 2022. Generalized and heterogeneous nonlinear dynamic multiagent systems using online RNN-based finite-time formation tracking control and application to transportation systems. IEEE Transactions on Intelligent Transportation Systems, 23, 13708–13720.

Li, D., Zhao, Y., Guo, S., Lin, F., Xu, T., 2025. Adaptive-neural-network-based robust hierarchical path-tracking control of autonomous vehicles considering parametric uncertainties and tire slip. Automotive Innovation, 8, 662–680.

Liu, P., Hao, Y., Wang, Q., 2024. Distributed formation-containment control of networked mobile robots using the Udwadia–Kalaba approach. IEEE Transactions on Network Science and Engineering, 11, 848–857.

Liu, Q., Wang, R., Cai, Y., Xiong, X., Chen, L., 2025. L3-AVs conflict risk prediction in highway maintenance areas using the CatBoost model and SHAP method explanation. Automotive Innovation, 8, 405–420.

Liu, Y., Zhou, A., Wang, Y., Peeta, S., 2025. Proactive longitudinal control to assist lane changes of human-driven vehicles in mixed traffic: human-emulation approach. Automotive Innovation, 9, 48–64.

Lu, S., Pan, M., Cheng, K., Sun, Q., 2024. A new saturation control for uncertain system using diffeomorphism approach: application to turbofan engine. IEEE Transactions on Industrial Informatics, 20, 8861–8872.

Pizetta, I.H.B., Brandão, A.S., Sarcinelli-Filho, M., 2019. Avoiding obstacles in cooperative load transportation. ISA Transactions, 91, 253–261.

Sun, Q., Wang, X., Yang, G., Chen, Y.-H., Ma, F., 2023. Adaptive robust formation control of connected and autonomous vehicle swarm system based on constraint following. IEEE Transactions on Cybernetics, 53, 4189–4203.

Udwadia, F.E., 2023. The general Gauss principle of least constraint. Journal of Applied Mechanics, 90, 111006.

Udwadia, F.E., Kalaba, R.E., 2002a. On the foundations of analytical dynamics. International Journal of Non-Linear Mechanics, 37, 1079–1090.

Udwadia, F.E., Kalaba, R.E., 2002b. What is the general form of the explicit equations of motion for constrained mechanical systems? Journal of Applied Mechanics, 69, 335–339.

Udwadia, F.E., Kalaba, R.E., Eun, H.-C., 1997. Equations of motion for constrained mechanical systems and the extended D'Alembert's principle. Quarterly of Applied Mathematics, 55, 321–331.

Wang, C., Ji, J., Miao, Z., Zhou, J., 2021. Synchronization control for networked mobile robot systems based on Udwadia–Kalaba approach. Nonlinear Dynamics, 105, 315–330.

Wang, F., Chen, K., Zhen, S., Chen, X., Zheng, H., Wang, Z., 2024. Prescribed performance adaptive robust control for robotic manipulators with fuzzy uncertainty. IEEE Transactions on Fuzzy Systems, 32, 1318–1330.

Yamashita, A., Arai, T., Ota, J., Asama, H., 2003. Motion planning of multiple mobile robots for cooperative manipulation and transportation. IEEE Transactions on Robotics and Automation, 19, 223–237.

Yang, S., Zhao, Z., Huang, Y., Fu, J., 2025. Robust constraint-following control for networked multiagent systems with uncertainties. IEEE Transactions on Systems, Man, and Cybernetics: Systems, 55, 272–283.

Yang, Y., Negash, N.M., Yang, J., 2025. Recent advances in interactive driving of autonomous vehicles: comprehensive review of approaches. Automotive Innovation, 8, 304–334.

Yang, Z., Huang, J., Yang, D., Zhong, Z., 2022. Design and optimization of robust path tracking control for autonomous vehicles with fuzzy uncertainty. IEEE Transactions on Fuzzy Systems, 30, 1788–1800.

Yin, H., Wang, N., Zhang, Z., 2025. Prescribed performance nonholonomic trajectory-tracking control of uncertain mechanical systems: a transformation-free approach. Nonlinear Dynamics, 113, 3421–3437.

Zhang, D., Zhang, Y., Zhang, H., Jia, C., Li, C., 2024. A generalized Udwadia–Kalaba control design for uncertain belt conveyor systems with inequality constraints. ISA Transactions, 151, 409–422.

Zhao, R., Li, M., Niu, Q., Chen, Y.-H., 2020. Udwadia–Kalaba constraint-based tracking control for artificial swarm mechanical systems: dynamic approach. Nonlinear Dynamics, 100, 2381–2399.

Zhao, X., Dang, B., Chen, Y.-H., Dong, F., Huang, J., 2026. A fuzzy-theoretic cooperative game framework for adaptive robust control of air–ground vehicle systems. IEEE Transactions on Fuzzy Systems, 34, 679–692.

Zhao, Z.L., Chai, T., Wei, C., Liu, D., Liu, T., Jiang, Z.P., 2021. Compensation-signal-driven control for a class of nonlinear uncertain systems. Automatica, 125, 109423.

Zheng, K., Zhou, B., Wu, X., Gan, N., Wei, W., 2025. Emergency collision avoidance system based on phase plane regression region. Automotive Innovation, 8, 712–723.

Zhu, Z., Ma, J., Wang, W., Xian, Y., Sun, H., Zhao, H., et al., 2023. Robust constraint-following control for uncertain mechanical systems with generalized Udwadia–Kalaba approach. IEEE Control Systems Letters, 7, 2263–2268.

Author biography

Xiaomin Zhao is currently an Associate Professor at the School of Automotive and Transportation Engineering, Hefei University of Technology, China. From 2013 to 2015, she was a jointly trained doctoral student at the Georgia Institute of Technology. She received the Ph.D. degree from Hefei University of Technology in 2017. Her research interests include system modeling, control theory, and vehicle engineering.

Bingwen Wang received the B.E. degree from the School of Mechatronic Engineering, Shenyang Aerospace University, Shenyang, China, in 2025. He is currently pursuing the M.S. degree at Hefei University of Technology. His research interests include intelligent systems control and vehicle dynamics and control.

Xinhua Gao is a Senior Engineer with Chery Automobile Co., Ltd., Wuhu, China. He is also an Industrial Professor at Hefei University of Technology. His e-mail address is gaoxinhua@hfut.edu.cn.

Weilong Hu is with Chery Automobile Co., Ltd., Wuhu, China. He is also a researcher at Hefei University of Technology. His e-mail address is huweilong@hfut.edu.cn.

Ye-Hwa Chen received the Ph.D. degree in Mechanical Engineering from the University of California, Berkeley, USA, in 1985. He is currently a Professor of Mechanical Engineering at the Georgia Institute of Technology, USA. His research interests include adaptive robust control, constraint management, and modular vehicles. He has published more than 320 peer-reviewed journal papers. He has received numerous research awards, including the Sigma Xi Outstanding Paper Award, the Sigma Xi Junior Faculty Award, the Georgia Tech Campanile Award, and the IEEE Transactions on Fuzzy Systems Outstanding Paper Award. He has served as a Regional Editor or Associate Editor for eleven international journals.